*J. Fluid Mech.* (1994), *vol.* 280, *pp.* 41–67



# Numerical and experimental investigations of low-density supersonic jets of hydrogen

By I. D. BOYD[1], D. R. BEATTIE[2] AND M. A. CAPPELLI[2]

[1] Cornell University, Ithaca, NY 14853, USA

[2] Stanford University, Stanford, CA 94305, USA

(Received 12 November 1993 and in revised form 10 June 1994)

Low-density flow of molecular hydrogen from a small nozzle is studied using numerical and experimental techniques. The conditions in the nozzle indicate that non-equilibrium effects will significantly influence the flow. Therefore, the numerical analysis is undertaken using a Monte Carlo approach. The experimental studies employ spontaneous Raman scattering. Comparisons of the measured data and computed results are made for total number density, rotational temperature, and for the number density of the first rotational level. The numerical results are found to be quite sensitive to the rotational relaxation rate, and a strong degree of thermal non-equilibrium is observed at the exit plane of the nozzle. Comparisons between experiment and analysis permit estimation of the rotational relaxation rate for hydrogen. Investigations are also conducted for expansion of the supersonic jet into a finite back pressure. The interaction of the plume with the chamber background gas is found to form shock waves in both the simulations and experiments. This phenomenon is investigated further by increasing the background pressure. Direct comparison of the simulation results and experimental measurements is very favourable.

## 1. Introduction

Low-power hydrogen arcjet propulsion engines are under development for use on spacecraft for orbit transfer and station-keeping manoeuvres. Potentially, these engines offer significant improvements in specific impulse over current chemical rockets. However, the thrust efficiencies achieved to date with these rockets have only reached about 30%. Many of the factors that cause this relatively low efficiency are concerned with the fluid mechanics and chemical kinetics of hydrogen. The purpose of the present study is to examine some of these effects at a fundamental level. Detailed studies are performed for flow of hydrogen in a small nozzle. The geometric size and mass flow are representative of a spacecraft thruster. These aspects combine to give a low Reynolds number in the nozzle throat that yields flow in strong thermodynamic non-equilibrium. In this paper, both numerical and experimental studies are reported for an unheated hydrogen flow. These represent the first phase of a continuing effort to investigate arc-heated expanding hydrogen flows. The experimental investigation employs Raman scattering to obtain number density and rotational temperature.

Sophisticated experimental techniques are being applied to investigate flow properties in the nozzle and plume of various arcjet thrusters. In these investigations, the thruster plume expands into a vacuum tank. Of course, owing to the finite pumping speeds of ground-based experimental facilities, the back pressures obtained are orders of magnitude higher than orbital flight conditions. There is an interest in understanding

how measurements taken in such facilities may be affected by the interaction of the expanding thruster plume with this residual pressure in the test chamber. This study addresses the issue for the hydrogen thruster operated in the arcjet facility at Stanford University.

Unfortunately, it is quite difficult to estimate such effects. The plume expanding from a typical arcjet is complicated by viscous and chemical kinetic effects. The flow field is two-dimensional such that densities at the nozzle exit centreline may be an order of magnitude higher than those at the nozzle lip. In addition, the physical behaviour that occurs in the interaction region between the plume and the residual gas is not simple. Depending on flow conditions, shock waves may be formed, and the viscous and kinetic effects again become significant. Therefore, a detailed study of the interaction phenomenon has been undertaken. Experimental investigations again employ Raman scattering to measure number density along the axis of the plume. The measurements are carried through the interaction region where the thruster plume encounters the residual gas. In addition, Monte Carlo calculations of the same flow conditions are performed.

Details of the experimental and numerical methods are provided in the following sections. In the numerical study, particular attention is given to the modelling of rotational relaxation for $H_2$. A description of the nozzle and plume flows is given, and comparison of the numerical results and experimental data is discussed.

## 2. Experimental investigations

This section describes experiments performed using spontaneous Raman scattering to determine the rotational-level populations of $H_2$ for the flow in the expansion plume of a small rocket. The theory of this technique is described first. Discussions then follow on the experiments performed, and the methods employed for interpretation of the results.

### 2.1. *Theory*

Spontaneous Raman scattering is an inelastic, linear, two-photon scattering process. In this case, an incident photon scatters off an $H_2$ molecule causing a change in the molecular quantum state and a corresponding change in the energy of the scattered photon. The intensity of the signal is given by Valentini (1987):

$$N_{i,f} = N_L l n_0 \frac{n(v_i, J_i)}{n_0} \left(\frac{\mathrm{d}\sigma}{\mathrm{d}\Omega}\right)_{i,f} \mathrm{d}\Omega, \tag{1}$$

where $N_{i,f}$ is the number of Raman photons collected for transition from initial state $i$ to final state $f$; $N_L$ is the number of incident laser photons; $l$ is the sample length imaged; $n_0$ is the number density of scattering species; $n(v_i, J_i)/n_0$ is the population fraction in state $i$; $v_i$ is the initial vibrational state; $J_i$ is the initial rotational state; $(\mathrm{d}\sigma/\mathrm{d}\Omega)_{i,f}$ is the differential Raman cross-section for transition from state $i$ to state $f$; and $\mathrm{d}\Omega$ is the collection solid angle.

The number of scattered photons is linearly proportional to the number of incident photons and the density of the scattering species. Spontaneous Raman scattering has the advantage of allowing spatially resolved measurements of ground-state densities with an easily interpretable signal. The primary disadvantage is the small scattering cross-section (typically $10^{-33}$ m$^2$). Measurements here are based on the purely vibrational Raman transitions from $v = 0$ to $v = 1$ with $\Delta J = 0$ for $J = 0$, 1, 2 and 3 (i.e. the Q-branch). Table 1 shows a summary of initial and final states, wavelength,

| $v_i$ | $v_f$ | $J_i$ | $J_f$ | $\lambda$ (nm) | $\sigma$ $10^{-33}$ m$^2$ | $n_i/n_0$ | Relative intensity |
|---|---|---|---|---|---|---|---|
| 0 | 1 | 0 | 0 | 612.325 | 1.544 | 0.128 | 1.982 |
| 0 | 1 | 1 | 1 | 612.103 | 1.648 | 0.657 | 10.828 |
| 0 | 1 | 2 | 2 | 611.662 | 1.645 | 0.117 | 1.930 |
| 0 | 1 | 3 | 3 | 611.004 | 1.665 | 0.092 | 1.529 |

TABLE 1. Summary of Raman transitions

cross-section, Boltzmann fraction, and relative intensity for these transitions using a laser wavelength of 487.986 nm and a gas temperature of 300 K.

The density can be determined by using the absolute intensity from all transitions combined in conjunction with the signal from a reference cell. The sum of the intensity of each transition divided by its cross-section is proportional to the density and a constant determined by the optical system:

$$\begin{aligned}\sum_i \frac{N_{i,f}}{(\mathrm{d}\sigma/\mathrm{d}\Omega)_{i,f}} &= \sum_i N_L l n_0 \frac{n(v_i, J_i)}{n_0}\mathrm{d}\Omega \\ &= N_L l n_0 \mathrm{d}\Omega \\ &= \alpha n_0. \end{aligned} \tag{2}$$

A spectrum recorded from a known gas density can be used to determine $\alpha$ and hence the density from subsequent spectra.

The relative intensity of the various transitions can be used to determine a rotational temperature, assuming partial thermodynamic equilbrium exists among the rotational states. The intensity of each transition divided by its cross-section is proportional to the density and the population fraction of the initial state:

$$\begin{aligned}\frac{N_{i,f}}{(\mathrm{d}\sigma/\mathrm{d}\Omega)_{i,f}} &= N_L l n_0 \frac{n(v_i, J_i)}{n_0}\mathrm{d}\Omega \\ &= \alpha n_0 \frac{n(v_i, J_i)}{n_0} \\ &= \alpha n_0 f(T, i). \end{aligned} \tag{3}$$

When two or more transitions are observed, their intensities can be fitted to a function of temperature and density (using the predetermined optical system constant).

### 2.2. *Experiments*

The nozzle considered in the present study is based on a 1 kW class NASA hydrogen thruster. The converging–diverging nozzle geometry is shown in figure 1. Note the cathode that is present in the device. The nozzle has a 0.64 mm throat diameter with a 20° half-angle, and an exit-to-throat area ratio of 225:1. The conditions chosen for examination represent a cold-flow configuration in which the arc is not ignited. The specific flow conditions are a stagnation temperature of 295 K and a mass flow rate of 14.1 mg s$^{-1}$. These conditions correspond to a Reynolds number at the nozzle throat of about 2800. This value indicates that the flow is dominated by the effects of thermal relaxation, and by viscosity in the nozzle boundary layer. The thruster is operated in a vacuum chamber 1.09 m long and 0.56 m in diameter with optical access through 75 mm diameter ports. It is mounted on a two-axis translation stage (axial and radial).

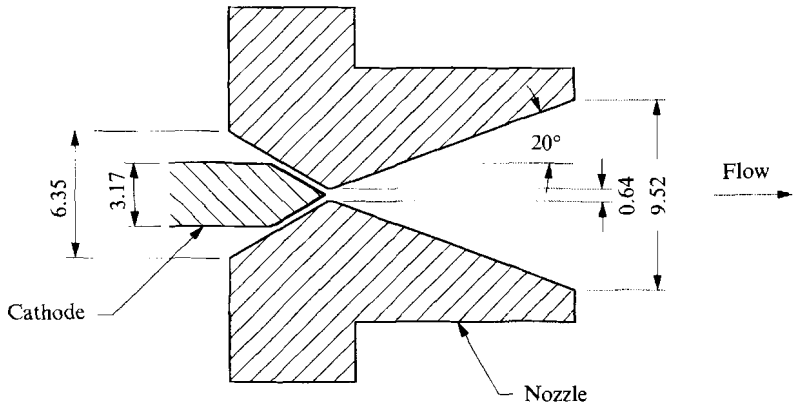


FIGURE 1. Nozzle geometric configuration (dimensions in mm).

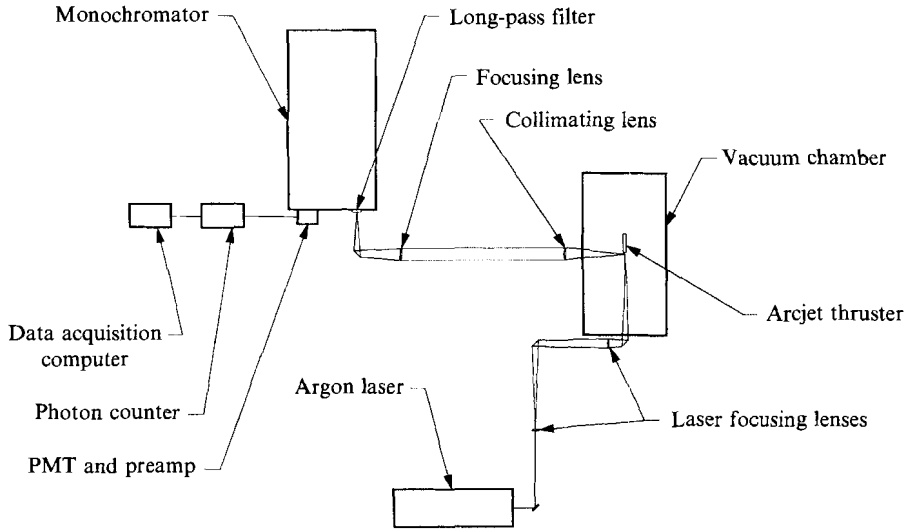


FIGURE 2. Experimental apparatus.

The tank is evacuated by two Roots blowers backed by mechanical roughing pumps with a total capacity of $1.2\ m^3\ s^{-1}$. This system is capable of maintaining a back pressure of $43 \pm 2$ Pa with a flow rate of $14.1 \pm 0.1\ mg\ s^{-1}$.

The Raman excitation source is an $Ar^+$ laser with 2.5 W in the 487.986 nm line used for this experiment. The laser beam is focused axially into the plume with a beam waist under 100 μm (see figure 2). Scattered light is collected and focused onto a monochromator entrance slit with an achromatic two-lens system. The collection optical axis is perpendicular to the laser polarization and the direction of laser propagation. The spatial resolution is 4 mm in the axial direction (determined by the slit height) and 0.1 mm in the radial direction (determined by the laser beam waist). The monochromator is a 1.0 m focal length f/8.7 single-pass Czerny–Turner design with a 1180 line $mm^{-1}$ grating blazed at 500 nm. A long-pass filter is placed before the entrance slit to further reduce the intensity of collected laser light to negligible levels. The monochromator slits are typically 300 μm giving a spectral resolution of 0.2 nm.

Light is detected at the exit slits by a cooled low-noise photomultiplier tube (PMT) with dark noise of 0.4 counts $s^{-1}$. The PMT output is amplified and sent to a

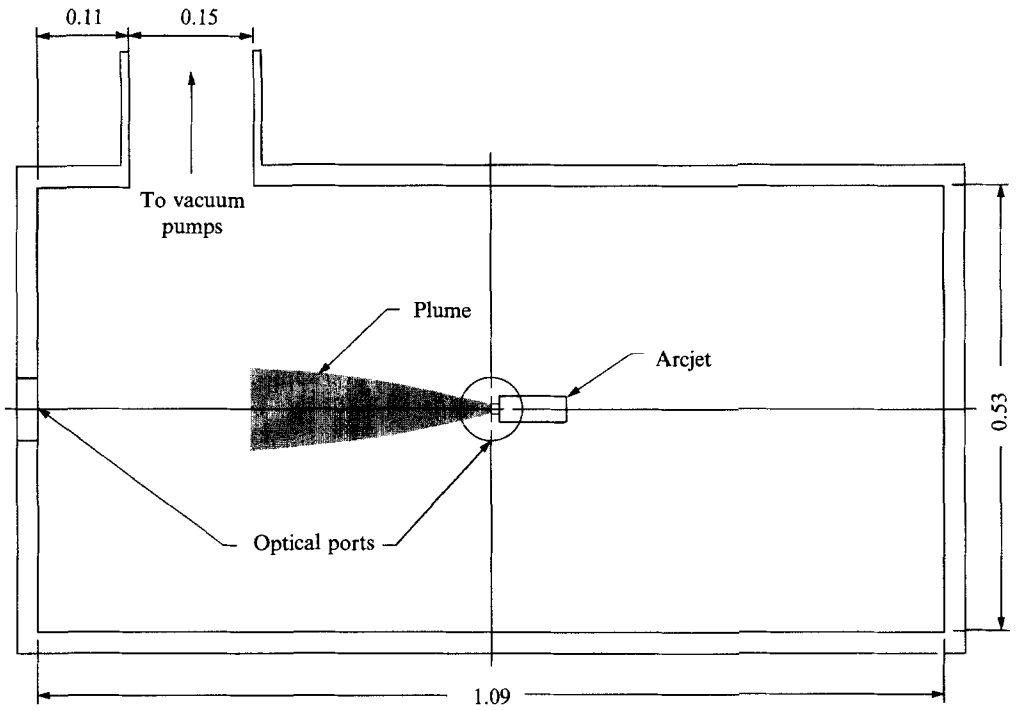


FIGURE 3. Schematic of arcjet in vacuum chamber (dimensions in m).

continuously gated photon counter. The monochromator is scanned over the spectral ration of interest and the photon counter output is recorded on a computer. The signal intensity is calibrated by filling the chamber with 10 kPa of $H_2$. A spectral scan is recorded with the operating conditions unchanged from those used for the data scans.

The overall experimental configuration is shown schematically in figure 3. Of particular interest is the position of the vacuum pumps with respect to the expanding flow. The location of the pumps will clearly give a non-symmetric background pressure field. It is presumed that such effects are small given the relatively large distance of separation between the pumps and the arcjet.

### 2.3. *Data analysis*

Spectral scans of the Raman Q-branch are recorded at various radial positions from the centreline to the nozzle edge. The collection segment starts at the nozzle exit plane and extends 4 mm downstream. Scans are also made on the centreline at various axial positions. The total number of scans taken is limited by the somewhat long scan duration of 40 minutes at 0.05 nm $min^{-1}$. In order to provide a more detailed view of the flow profile in the exit plane, data are also collected at a fixed spectral position while scanning the axial position.

The spectral data are analysed by fitting to theoretical spectra with the unknown quantities such as temperature and density as fitting parameters. The theoretical spectra are obtained by calculating the predicted position and intensity of the various Q-branch lines, then convoluting with the instrument response function. The line positions are taken from the experimental values of Veirs & Rosenblatt (1987) which are in excellent agreement with the quantum mechanical calculations of Wolniewicz (1983). The line intensities are proportional to the Boltzmann fraction in the initial

state and the transition Raman cross-section. The cross-sections are taken from the dynamic polarizability calculations of Ford & Brown (1973). Since these values are averaged over all solid angles for unpolarized light, it is assumed that any variations with solid angle or polarization are the same for all Q-branch transitions. Note that the Ford & Brown cross-sections are defined in terms of scattered energy rather than scattered photons, as defined in (1). The two definitions differ by a factor of $\lambda_s/\lambda_0$, where $\lambda_s$ is the scattered wavelength and $\lambda_0$ is the incident wavelength.

As expected, the observed spectral features are principally instrument broadened. The Raman transitions are primarily Doppler broadened at the low pressures involved. According to Weber (1973), the Doppler width (FWHM) is

$$\Delta\nu_D = \frac{2}{c}\left(2\ln 2\frac{kT}{m}\right)^{1/2}\left[4(\nu_0^2+\nu_0\nu_R)\sin^2\frac{\theta}{2}+\nu_R^2\right]^{1/2}, \tag{4}$$

where $T$ is the gas temperature = 300 K; $m$ is the hydrogen molecule mass; $\nu_0$ is the incident photon frequency; $\nu_R$ is the Raman frequency shift; and $\theta$ is the collection angle = 90°.

Using (4), a value of 3.57 GHz is obtained for $\Delta\nu_D$. This Doppler width of 4.5 pm and the laser linewidth of 5 pm are both small in comparison to the 0.2 nm monochromator resolution. Hence the monochromator slit function is used to represent the instrument function for fitting purposes. Since the monochromator slits are equal in width and the resolution is large compared to the diffraction limit (0.01 nm), a triangular function is utilized.

Two fits are performed. The first fit, NTE (Non-Thermodynamic Equilibrium), does not assume that the flow is in thermodynamic equilibrium. The rotational population fractions (and thereby relative intensity of the transitions) are freely varied to best fit the data. Additional fit parameters include a wavelength offset to account for monochromator error, an intensity offset to allow for PMT dark noise, and the width of the slit function.

The second fit (LTE) assumes that the flow is in local thermodynamic equilibrium (LTE) with a rotational temperature dictating the rotational population fractions. The two parameters in this fit are the temperature and number density. The wavelength offset, intensity offset and spectral resolution have the same values determined by the NTE fit. The rotational energy levels used to compute the Boltzmann fractions are calculated with a six-parameter fit from Jennings, Rahn & Owyoung (1985). This fit is in excellent agreement with the energy level calculations for $J = 0, 1, \ldots, 5$ of Wolniewicz (1983). The vibrational partition function is calculated assuming a harmonic oscillator using the energy difference from $v = 0$ to $v = 1$ also provided by Wolniewicz. The harmonic approximation introduces negligible error in absolute intensity since the population fraction in the ground state is close to unity at the low temperatures of this study.

At the low temperatures involved here, the symmetric/antisymmetric nuclear spin states of $H_2$ do not reach equilibrium. This equilibration process can be extremely slow in the absence of a catalyst (McQuarrie 1973). Owing to the coupling of nuclear and rotational spin states, this non-equilibrium results in the rotational populations deviating from a Boltzmann distribution. Since H nuclei have spin $\frac{1}{2}$ (i.e they are fermions), $H_2$ must have an antisymmetric total wave function:

$$\Psi_{total} = \Psi_{trans}\,\Psi_{rot}\,\Psi_{vib}\,\Psi_{elec}\,\Psi_{nuclear}. \tag{5}$$

The only components of the total wave function which can be antisymmetric are the nuclear and rotational wave functions (see table 2). Therefore, an $H_2$ molecule must

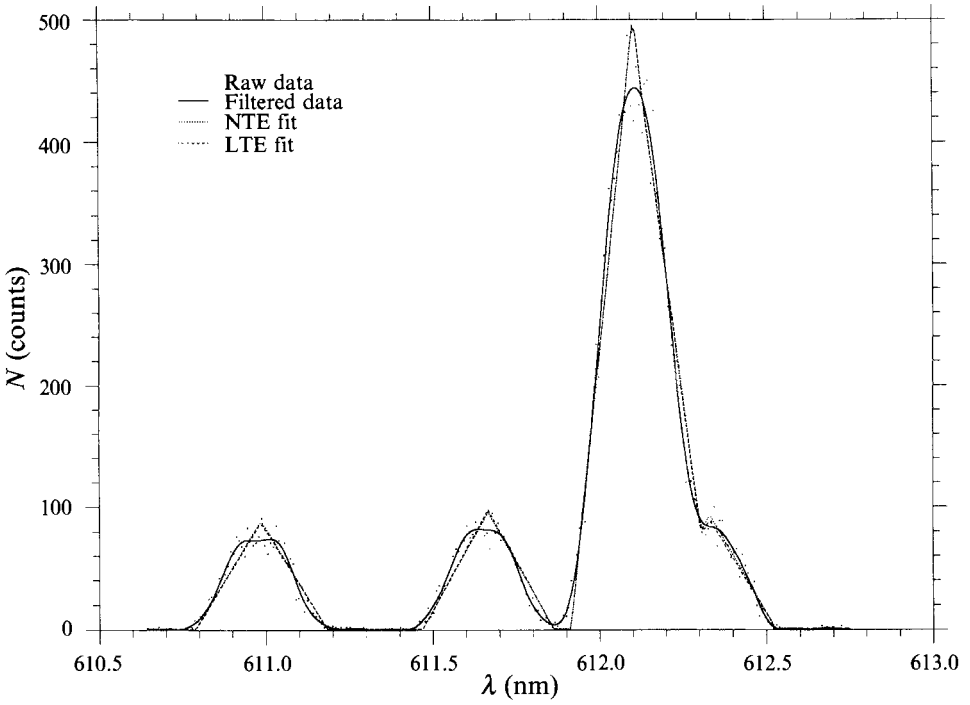


FIGURE 4. Scan of Raman intensity against wavelength taken under reference conditions.

| Wave function | Symmetry | Degeneracy |
|---|---|---|
| Translational | Symmetric | 1 |
| Rotational | | |
| $J$ even | Symmetric | $2J+1$ |
| $J$ odd | Antisymmetric | $2J+1$ |
| Vibrational | Symmetric | 1 |
| Electronic: $^1\Sigma_g^+$ | Symmetric | 1 |
| Nuclear | | |
| Ortho | Symmetric | 3 |
| Para | Antisymmetric | 1 |

TABLE 2. $H_2$ wave function

be in a symmetric nuclear state and antisymmetric rotational state or vice versa. These two combinations are often referred to as ortho and para respectively. The nuclear degeneracy ratio of 3:1 (ortho–para) results in a 3:1 statistical weighting of odd–even $J$ states. Above 300 K, the upper rotational states are sufficiently populated in a Boltzmann distribution that the ortho–para ratio is in fact 3:1. However, at lower temperatures where the population increasingly fills $J = 0$, the ortho–para ratio decreases. In the limit as $T$ approaches 0, the equilibrium ortho–para ratio also approaches zero.

The implication of this phenomenon is that equilibrium dictates an ortho–para ratio below 3:1 at the temperatures in this flow. However, since the ortho–para ratio is frozen at the 3:1 high-temperature limit, the rotational population fractions will not be Boltzmann, even if the rotational states are in LTE. This effect is accounted for in the fitting process by upholding the 3:1 ortho–para ratio, while at the same time

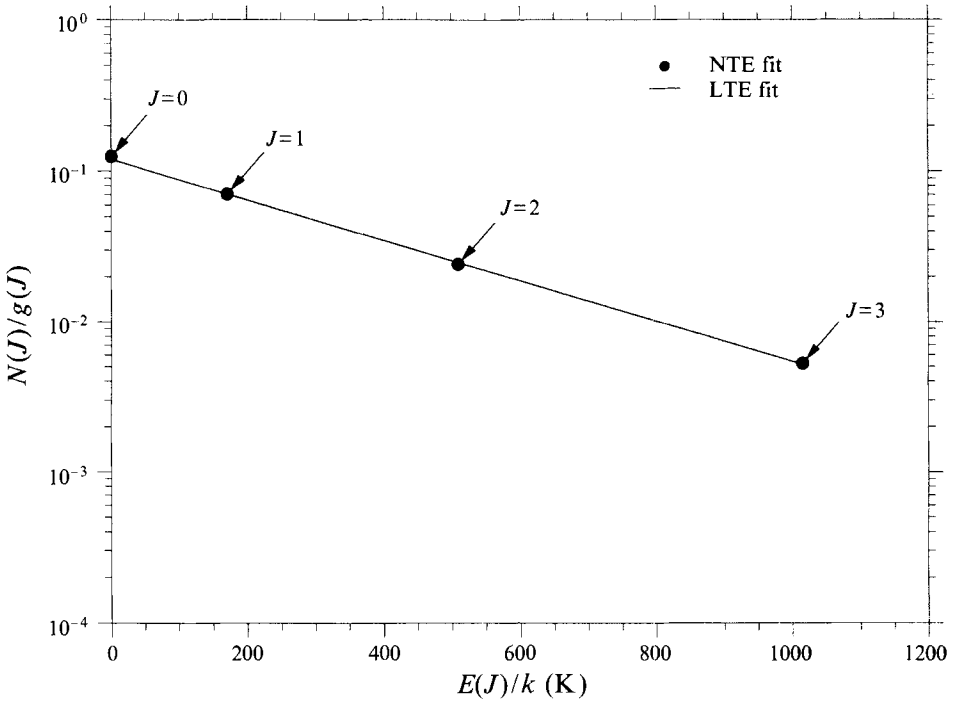


FIGURE 5. Boltzmann plot of rotational population under reference conditions, $T = 323 \pm 1$ K, $n = (2.27 \pm 0.02) \times 10^{24}$ m$^{-3}$.

requiring that the odd and even states independently satisfy a Boltzmann distribution with the same rotational temperature. On a Boltzmann plot, the odd and even states each fall on a line with the same slope (i.e. same temperature) but a different intercept. As the temperature is decreased the intercepts move further apart.

In order to measure absolute density, reference scans are taken with the tank containing 10 kPa of hydrogen. A sample reference scan showing the raw data, filtered data, NTE fit, and LTE fit is shown in figure 4. The raw data are low-pass filtered to allow the spectral features to be seen more clearly. Fitting to the raw data and filtered data is found to give identical results. The two fits agree quite well, as expected, since the gas should be in equilibrium. A Boltzmann plot of the results from the two fits shows that the data match the equilibrium fit to within experimental error (figure 5).

A scan taken in the exit plane of nozzle is shown in figure 6. The intensity is lower than the reference intensity and the shot noise is much more evident. It is also clear that the population has shifted almost entirely into the $J = 0$ and $J = 1$ states, indicating a lower temperature. The LTE fit temperature was $113 \pm 5$ K. From the Boltzmann plot shown in figure 7, one can see the equilibrium fit lines match the $J = 0$, 1, and 2 intensities quite well. The discrepancy between the equilibrium and non-equilibrium fits at $= 3$ is not surprising since the signal-to-noise ratio of that data point is very poor ($< 1$).

The calculation of number density is slightly more accurate than temperature, especially at the lower signal levels. The cross-sections of interest are almost equal, so it is not critical that the fitting process determine exactly what portion of the overlapping peaks corresponds to $J = 0$ and $J = 1$. However, the error in density of the data scan is the sum of the density parameter fitting error and the reference density error.

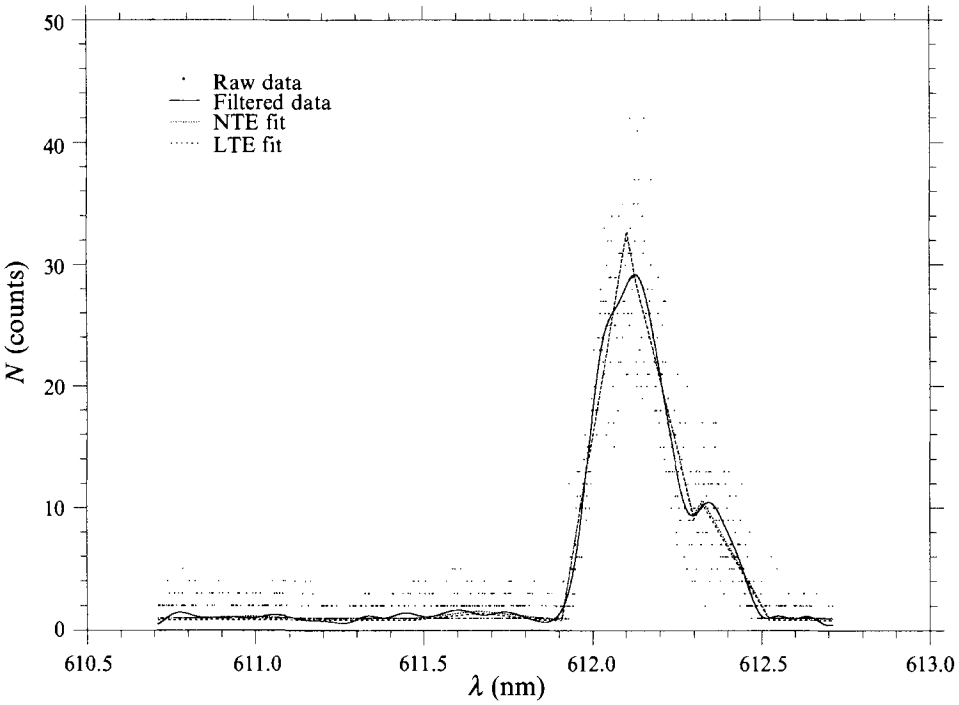


FIGURE 6. Scan of Raman intensity against wavelength taken in the nozzle exit plane.

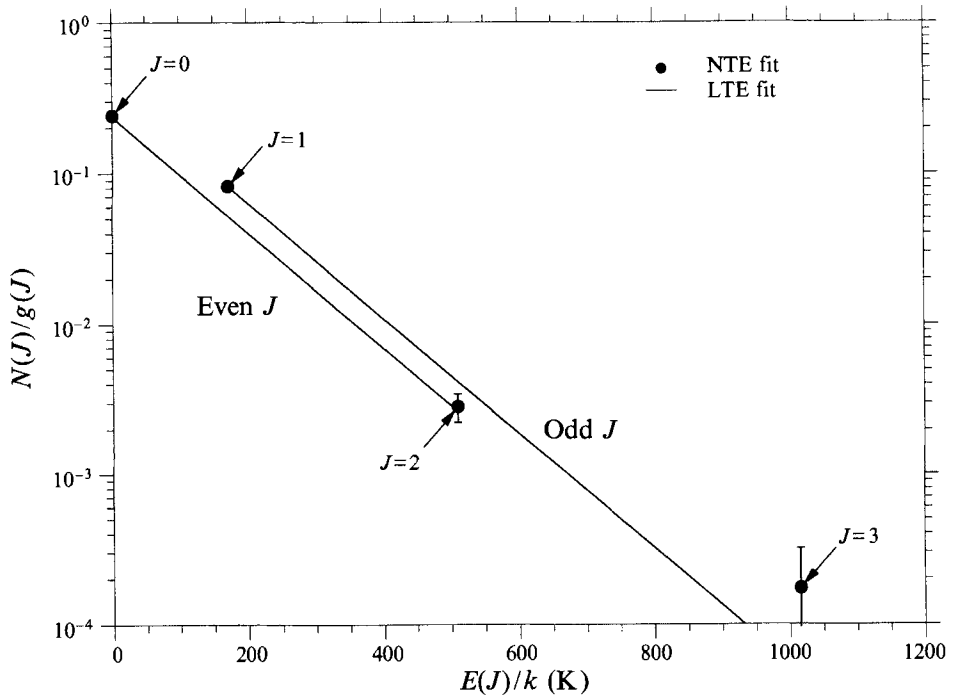


FIGURE 7. Boltzmann plot of rotational population taken in the nozzle exit plane, $T = 113 \pm 5$ K, $n = (6.15 \pm 0.15) \times 10^{22}$ m$^{-3}$.

A more detailed view of the exit-plane flow profile is obtained by setting the monochromator at the $J = 1$ peak and scanning the flow position radially. For this step, spectral resolution is less important, so the slits are opened to 400 μm to maximize the signal. This signal is proportional to the population in the $J = 1$ state, so it is normalized by the $J = 1$ signal from the spectral scans to give the density of state $J = 1$.

For the experimental data taken along the plume centreline, again the signal from the $J = 1$ state is measured. In this study, data are taken along the arcjet axis from the exit plane to 60 mm downstream. The back pressure in the vacuum tank is varied from 43 to 67 Pa by varying the number of pumps used. Data are also taken with the chamber evacuated below 1 Pa to give a background signal, and filled with 10 kPa hydrogen for a reference signal. The plume density is found by subtracting the background signal from the measured signal, then scaling by the known density of the reference scan. The error in density is estimated as one standard deviation, assuming that the counts follow a Poisson distribution. The errors range from 6% at the highest densities to 36% at the lowest.

## 3. Numerical investigations

This section discusses the numerical and physical aspects of simulating the flows of hydrogen using a Monte Carlo method. The general methodology for simulating the nozzle flow is described, details of the kinetics models employed are provided, and the rocket plume simulations are described.

### 3.1. *Nozzle flow simulation*

The low Reynolds number at the nozzle throat indicates that thermal non-equilibrium effects may be significant in the nozzle flow. The local value of the Reynolds number at the nozzle exit will be reduced by a factor close to the ratio of the exit and throat areas. Under such conditions, it is well established that the Navier–Stokes equations are invalid, owing to the failure of the linear forms for viscosity and thermal conductivity. A previous investigation of a small nitrogen thruster with a throat Reynolds number of 850 was reported by Boyd *et al.* (1992). In that investigation, experimental measurements of Pitot pressure were compared to continuum calculations at the nozzle exit. It was found that the continuum method overpredicted the pressure by 25%. An alternative numerical methodology for low-Reynolds-number flows is the direct simulation Monte Carlo method (DSMC) developed by Bird (1976). Instead of solving an equation set, this method attempts to provide a direct simulation of the flow by employing a large number of model particles. Boyd *et al.* (1992) employed this method and found it to give excellent agreement with the experimental data. Further studies by Penko *et al.* (1993) and Boyd, Jafry & Vanden Benkel (1994) have shown that the DSMC technique gives good agreement with experimental data taken in low-Reynolds-number plumes.

In a similar way to the previous study on $N_2$, the DSMC computation begins at the nozzle throat and extends out to the near field of the plume. Initially, throat profiles obtained from a Navier–Stokes solution of the flow were employed to begin the DSMC simulation. However, it was subsequently found that simple isentropic theory could be used without affecting the final DSMC solution far downstream of the throat. The interaction of the gas with the nozzle wall is assumed to be diffuse with full accommodation to a temperature of 300 K. In the study by Boyd *et al.* (1992) it was found that a temperature gradient existed along the nozzle wall. Such data were not

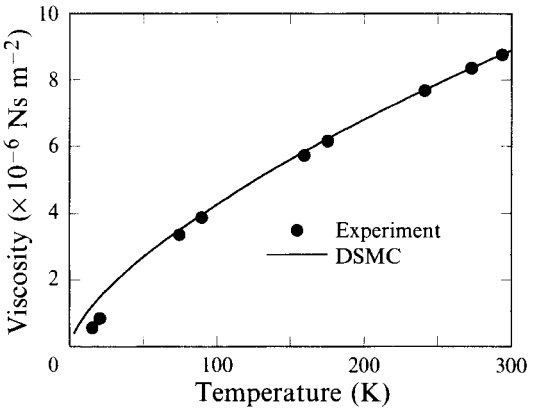


FIGURE 8. Temperature dependence of the viscosity coefficient for molecular hydrogen.

available for the present study and the assumption of a constant wall temperature may introduce a small error in the numerical results. For the nozzle simulation, the expansion of the plume is assumed to occur in a perfect vacuum. The computational grid employed in the present studies consists of 781 cells in the axial direction and 60 cells in the radial direction. The cell dimensions are varied with local flow conditions to maintain a maximum dimension of one local mean free path everywhere in the domain. In the important regions next to the nozzle wall and at the nozzle lip the cell sizes employed are much smaller than the local mean free path to obtain better resolution. An example of the type of grid employed in the present study is shown in Boyd *et al.* (1994). At the steady stage of the calculation there are about 700000 particles in a typical simulation. For this configuration, a typical run time is about 1.5 CPU hours on a Cray C-90.

### 3.2. *Hydrogen kinetics models*

Model parameters for translational and rotational relaxation must be chosen to apply the DSMC technique to low-temperature flows of molecular hydrogen. The stagnation conditions investigated indicate that it is only necessary to consider temperatures close to 300 K. Relaxation of the translational mode occurs in the simulation through collisions between particles. These collisions are computed by applying collision probabilities to pairs of particles in each cell in the computational domain. In the current study, the form of the collision probability is determined by the Variable Hard Sphere (VHS) model of Bird (1981). In this model, the important parameters are a reference collision diameter $d_{ref}$ and a viscosity temperature coefficient $\omega$. These parameters are obtained simultaneously by considering the temperature dependence of the coefficient of viscosity for hydrogen. In figure 8 experimental data for viscosity are compared to the VHS model using parameters $d_{ref} = 2.88 \times 10^{-10}$ m and $\omega = 0.67$. These are the values given by Bird (1981) for hydrogen and clearly give an excellent fit to the measured data.

In the DSMC method, relaxation of the rotational mode occurs by applying a probability of exchanging energy between the translational and rotational modes of particles that collide. For many diatomic species, a suitable energy-dependent form for this probability has been developed by Boyd (1990). The form of this probability reflects the observations made experimentally that the probability of rotational equilibration increases as temperature decreases. However, this trend appears to be reversed for diatomic hydrogen. In fact, the number of collisions required to equilibrate

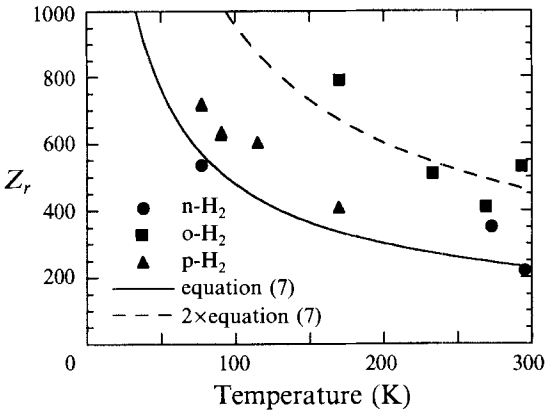


FIGURE 9. Temperature dependence of the rotational collision number for various forms of molecular hydrogen.

the rotational mode of this species increases as the temperature is decreased. This point is illustrated in figure 9 where the rotational collision number for three different forms of hydrogen are shown as a function of temperature. The experimental data are taken from literature cited by Lambert (1977). As discussed previously, the rotational state of hydrogen occurs in two different forms: para (p-$H_2$) and ortho (O-$H_2$). Under normal conditions (n-$H_2$), ortho-$H_2$ is present as 0.75 and para-$H_2$ is 0.25 by mole fraction.

Because the behaviour of $H_2$ differs from other diatomics, it is necessary to develop a new rotational energy exchange probability for the DSMC technique. In addition to the experimental data shown in figure 9, the available literature (Boitnott & Warder 1971; Lensch & Gronig 1977; Gallagher & Fenn 1974) indicates that the rotational relaxation time of hydrogen at temperatures below 300 K is within a factor of 2 of $\tau_r = 10^{-8}$ s at a pressure of 1 atmosphere. The definition for the rotational collision number is

$$Z_r = \tau_r/\tau_c, \tag{6}$$

where $\tau_c$ is the inverse of the molecular collision rate. Evaluating $\tau_c$ using the VHS model, and using a slightly higher value for the rotational relaxation time of $\tau_r = 1.4 \times 10^{-8}$ s, it may be shown that the rotational collision number for hydrogen is

$$Z_r = 10480/T^{\omega}. \tag{7}$$

This analytical form is compared to the available experimental data in figure 9. The simple model gives good agreement with the experimental data for normal hydrogen. By multiplying (7) by a factor of 2, good agreement is obtained for the experimental data for o-$H_2$. These comparisons give an idea of the spread in the available experimental data. Of course, this rather simple approach only gives an estimate of the rotational relaxation rate. Future studies may attempt to include more detailed analysis.

By following a similar analysis to that presented in Boyd (1990) for other diatomic species, it may be shown that the appropriate energy-dependent form of the probability of rotational energy exchange to be used in the DSMC technique based on (7) is

$$\phi_r = \frac{1}{Z_r} = \frac{1}{10480} \frac{\Gamma(\zeta + \frac{5}{2} - \omega)}{\Gamma(\zeta + \frac{5}{2})} \left(\frac{E_c}{k}\right)^{\omega}. \tag{8}$$

In (8), $E_c$ is the total collision energy, $k$ is the Boltzmann constant, and $\zeta$ is the average number of degrees of freedom participating in the energy exchange process ($\zeta = 2$ for a collision between two diatomic molecules that both exchange rotational energy in the collision). Because of its approximate nature, the leading constant in (8) is considered a parameter to be identified by comparison with the experimental data generated in this investigation.

Two separate adjustments must be made to (8) before it can be applied in the DSMC technique. The first is due to the implementation of collision mechanics. It has been shown by Lumpkin, Haas & Boyd (1991) that if the rotational energies of two particles are changed simultaneously in one collision then the probability must be multiplied by a factor

$$F_1 = \frac{5-2\omega+2\zeta}{5-2\omega}. \tag{9}$$

The second adjustment is due to the fact that the collision time given by the VHS collision model is not generally the same as that employed in converting experimentally measured rotational relaxation times to rotational collision numbers. In this conversion process, it is common (Parker 1964) to employ a collision time of the form

$$\tau_c = \pi\mu/(4p), \tag{10}$$

where $\mu$ is the coefficient of viscosity, and $p$ is the pressure. Accounting for the viscosity and collision time produced by the VHS model (Bird 1981) the following correction must be applied to (8):

$$F_2 = \frac{8\Gamma(\frac{9}{2}-\omega)}{15\pi\Gamma(\frac{5}{2}-\omega)}\frac{208-12\omega}{211-12\omega(\frac{5}{2}-\omega)}. \tag{11}$$

In the current application, with $\omega = 0.67$, and $\zeta = 2$, (9) and (11) are evaluated as $F_1 = 2.093$ and $F_2 = 0.870$ respectively. The probability of exchanging translational and rotational energy for each collision is then given by

$$\phi_r = F_1 \times F_2 \times \text{equation (8)}. \tag{12}$$

### 3.3. *Plume flow simulation*

The code employed in the nozzle study is based on a numerically efficient program designed to be executed on Cray supercomputers (Boyd 1991). With minor modifications, the same code is used in the plume study on a computer work-station. The rate of execution of the code on the work-station is ten times slower than on a Cray YMP.

Application of the DSMC technique to model the nozzle and near-field plume expansion of this unignited hydrogen arcjet is discussed above. The hydrogen kinetics model described above is again employed in the plume study. The flow field considered begins at the exit plane of the nozzle and extends to distances of 10 cm axially and 6 cm radially. The results computed for the nozzle flow are employed as an input condition at the nozzle exit plane for the present study. Decoupling the nozzle and plume calculations saves a great deal of computational expense. The densities in the nozzle flow are orders of magnitude higher than those occurring in the plume. The computational expense of the DSMC method is approximately proportional to the density of the flow. Therefore, it takes much less computer resources to perform a plume calculation. The smaller size of the plume problem allows the simulation to be performed in reasonable times on the work-station. The decoupled approach for

simulating nozzle and plume flows using the DSMC technique has been successfully applied in previous investigations (Boyd *et al.* 1992; Penko *et al.* 1993). It is observed that only at the highest chamber pressure considered below is there a very small upstream influence. The decoupled approach appears to be valid at least for the conditions considered in this study.

Boundary conditions are applied along the radial line directly above the nozzle lip, and along the maximum axial and radial coordinates of the computational domain (at $Z = 10$ cm and $R = 6$ cm respectively). In each case, these are specified in terms of pressure and temperature. It is very difficult to perform an exact simulation of the chamber residual pressure. As illustrated in figure 3, the pressure is not distributed homogeneously throughout the chamber. Also, it is not clear what the temperature of the residual gas will be. For the purposes of the present investigation, a constant pressure ($p_b$) for the background gas is assumed at each of the boundaries. In addition, the residual gas is assumed to be at room temperature (300 K). Particles are introduced into the simulation across each boundary with properties corresponding to a gas at rest at the conditions of the residual gas defined in this manner. This technique was applied in a previous investigation of helium micro-thrusters (Boyd *et al.* 1994), and diffuse shock-like structures were observed in the solutions. However, no experimental data were available to assess the validity of those calculated results.

## 4. Results

In this section, direct comparison is provided of the experimental data and numerical results obtained in this study. The comparisons are divided into those for nozzle and those for plume flow.

### 4.1. *Nozzle flow*

Flow-field properties predicted by the DSMC method are first considered before comparison with the experimental data is made. Contours of Mach number for the nozzle flow are shown in figure 10. It is noted that a very large viscous boundary layer develops in the nozzle flow such that only about 30% of the nozzle exit plane is isentropic. The DSMC method is found to successfully predict the important phenomenon at the nozzle lip which is intersected by the sonic line. This behaviour is not generally predicted by continuum methods and is due in part to the need to include slip effects along the nozzle wall. An idea of the degree of thermal non-equilibrium in the flow field is obtained from figures 11(*a*) and 11(*b*) where contours of temperatures obtained for the translational and rotational modes are shown. It is clear that the rotational mode relaxes at a significantly slower rate than the translational mode. These results are obtained using (12). It is concluded that rotational non-equilibrium plays an important role in the expansion of molecular hydrogen under conditions of low Reynolds number.

Comparison of numerical results and experimental data for total number density in the nozzle exit plane is made in figure 12(*a*). Three different DSMC solutions are shown corresponding to Case 1 using (12), Case 2 using half of (12), and Case 3 using twice (12) for the rotational relaxation rate of $H_2$. Note that Case 1 corresponds to the solid line given in figure 9 and Case 2 corresponds to the dashed line. Generally, the computational results for density are relatively insensitive to the exact form of the rotational relaxation rate, and quite good agreement with experiment is obtained. In both experiment and simulation a small drop in density close to the nozzle axis is observed. This is believed to be due to the influence of the thick viscous boundary layer that causes the gas on the centreline to expand more rapidly.

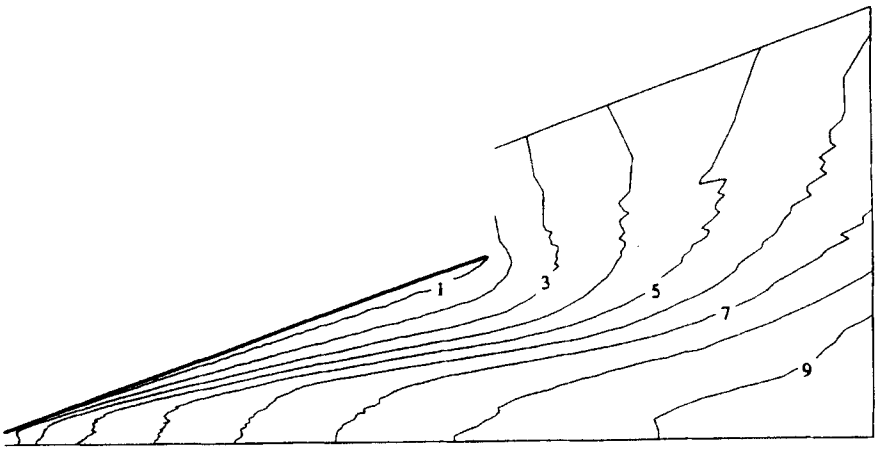


FIGURE 10. Contours of Mach number computed using the DSMC technique.

(*a*)

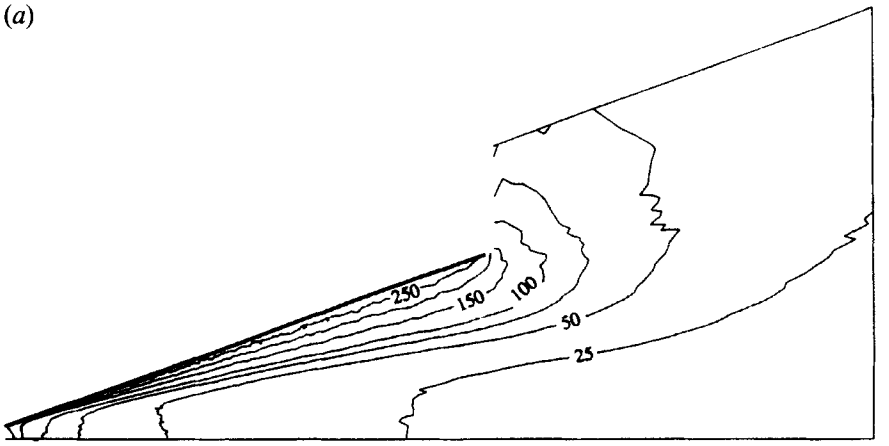


(*b*)

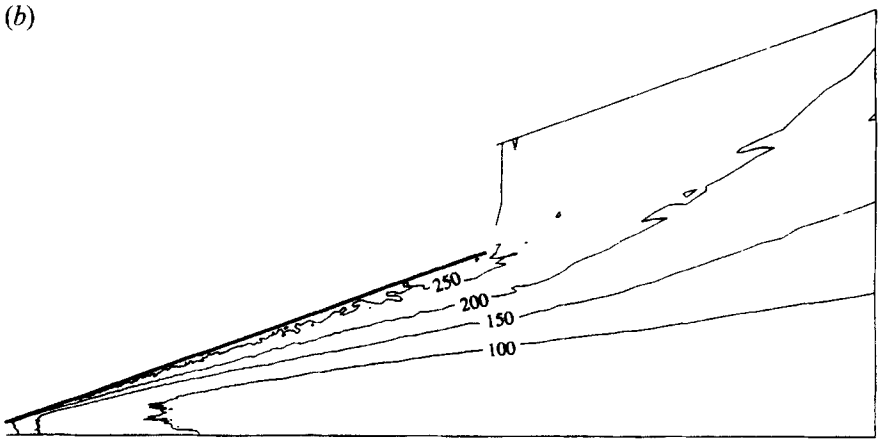


FIGURE 11. Contours of (*a*) translational and (*b*) rotational temperature, computed using the DSMC technique.

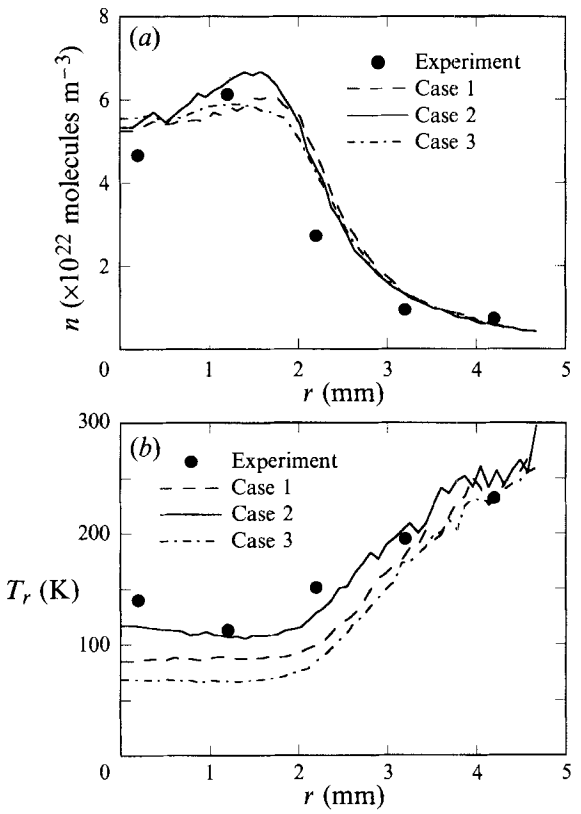


FIGURE 12. Comparison of experimental data and DSMC results for (*a*) number density and (*b*) rotational temperature in the nozzle exit plane.

Rotational temperature profiles in the nozzle exit plane are compared in figure 12(*b*). As might be expected, this quantity is much more sensitive to the probability employed for rotational equilibration. At the axis, there is a difference in rotational temperature of a factor of about 2 between Cases 2 and 3, corresponding to a difference in relaxation rate of a factor of 4. The best agreement with experiment is obtained for Case 2, the slowest rate considered. In agreement with the experimental data there is a small rise in rotational temperature at the nozzle axis. This makes physical sense considering the small decrease in density described previously. To display the significant degree of thermal non-equilibrium predicted by the DSMC method in the flow, the translational and rotational temperatures obtained in Case 2 are compared with the experimental data in figure 13. At conditions of thermal equilibrium, the rotational temperature could be combined with the number-density measurements to estimate the pressure in the nozzle exit plane using the equation of state. The DSMC analysis reveals that this procedure leads to errors in pressure on the axis of a factor of about 5. This observation provides a strong argument in favour of the need to perform detailed numerical simulations and to directly measure the gas kinetic temperature for these non-equilibrium flows.

The final comparison of results and data is for the number density of the first rotational level in the nozzle exit plane. These measurements are made at a finer spatial resolution than the total number density and rotational temperature measurements considered previously. The comparison is shown in figure 14. The DSMC results are

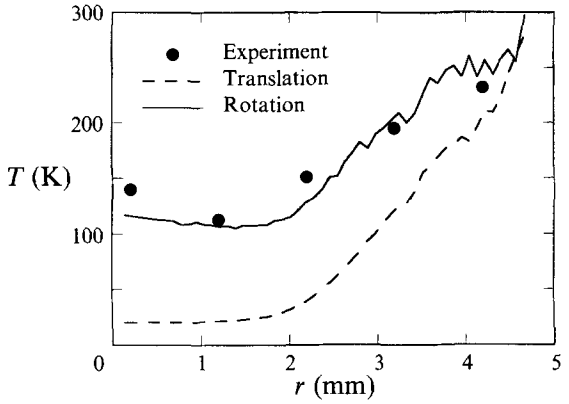


FIGURE 13. Degree of thermal non-equilibrium computed for Case 2 in the nozzle exit plane.

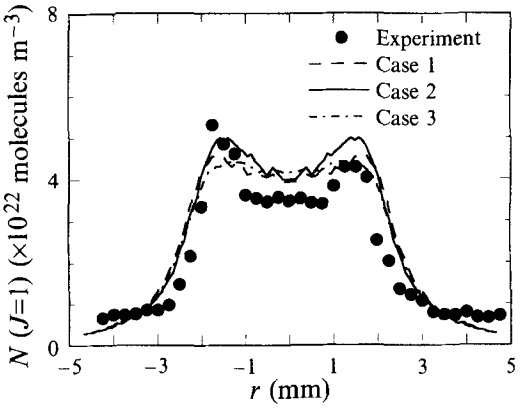


FIGURE 14. Comparison of experimental data and DSMC results for density of the $J = 1$ state in the nozzle exit plane.

computed from the values for total number density and rotational temperature in the exit plane. Note the small degree of asymmetry in the experimental data. The data on the left wing are in better agreement with those shown in figure 12. For this reason, it is concluded that the best comparison of theory and measurement occurs for Case 2. The good agreement obtained using this probability function for the three different data sets allows a value to be estimated for the rotational relaxation rate of hydrogen at temperatures below 300 K. When the probability used in Case 2 is converted into a relaxation time the value is $\tau_r p = 2.8 \times 10^{-8}$ s atm. This value is higher than those generally quoted for the relaxation of normal hydrogen. Recalling that a constant rotational relaxation time was employed in the analysis for temperatures below 300 K, this higher value may indicate that there is an increase in $\tau_r$ at low temperatures. On the other hand, this value is consistent with the experimental measurements for ortho-hydrogen. It is concluded that the relaxation time obtained in the present study is at least within the range of experimental data reported previously in the literature. The value obtained in the present study is a more complete test of the relaxation model due to the two-dimensional, viscous, and rapid-expansion processes experienced in the flow.

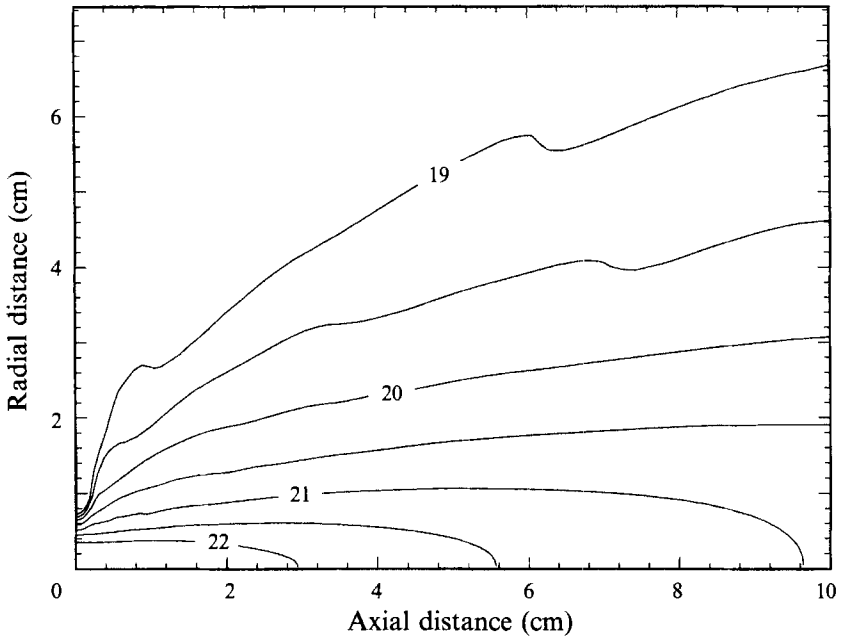


FIGURE 15. Contours of $\log_{10}$ number density in molecules $m^{-3}$ at a background pressure of 0 Pa.

### 4.2. *Plume flow*

First, the DSMC method is applied to model the hydrogen-plume expansion process into a perfect vacuum. This is similar to the in-flight operational mode of the device (although here the arc is unignited). The boundary conditions are therefore specified as $p_b = 0$ Pa. Contours of number density are shown in figure 15. Note that the nozzle exit is about 4.75 mm long, and the origin is at the nozzle exit. It is clear that the flow is highly directed. The variation of density along the plume centreline is shown in figure 16(*a*). The density decreases rapidly by a factor of about 50 at a distance of 10 cm from the nozzle exit. A significant decrease in the translational temperature is shown in figure 16(*b*). The translational temperature shown in figure 16(*b*) is a weighted average of the single mode parallel to, and the two modes perpendicular to, the flow direction. While the former mode is frozen due to lack of collisions, the latter modes continue to decrease due to geometric effects. Specifically, as the distance away from the source of a highly expanded, low-density jet increases, the molecules located on the centreline tend to have smaller and smaller velocity components perpendicular to the flow direction. This is because only those molecules with such velocity components have not moved far away from the centreline during the expansion process. Thus, when the frozen parallel velocity component is combined with the slowly decreasing perpendicular components, the overall translational temperature continues to decrease as shown in the computations. Also included in figure 16(*b*) is the rotational temperature which is frozen. Note the degree of thermal non-equilibrium that exists at the nozzle exit plane which occurred during the nozzle expansion process.

The lowest value of the residual chamber pressure that can be achieved in the experimental facility is $p_b = 43$ Pa. Contours of number density in particles $m^{-3}$ obtained using the DSMC technique for this condition are shown in figure 17. The finite chamber pressure creates a very thin jet with a diameter of about 1 mm. The diagram illustrates the important features that are typical of those observed in all

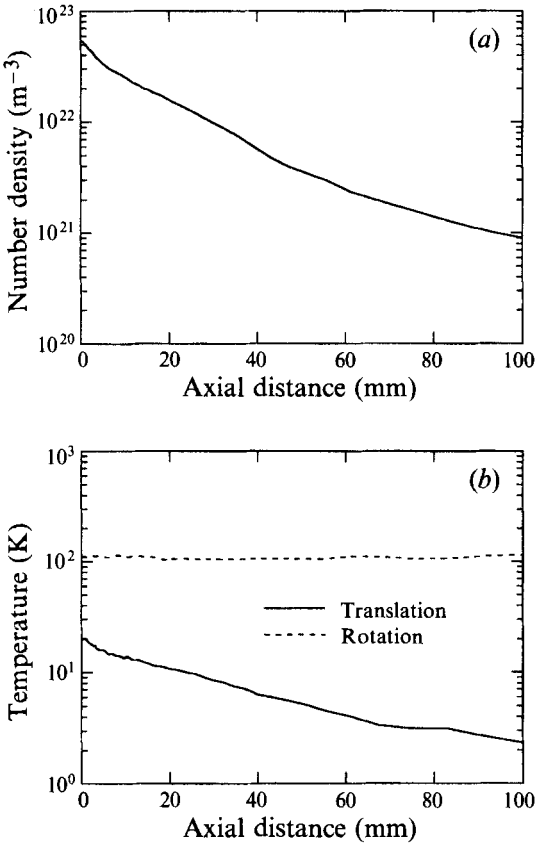


FIGURE 16. (*a*) Number density and (*b*) translational and rotational temperature, along the plume centreline computed with the DSMC method at a background pressure of 0 Pa.

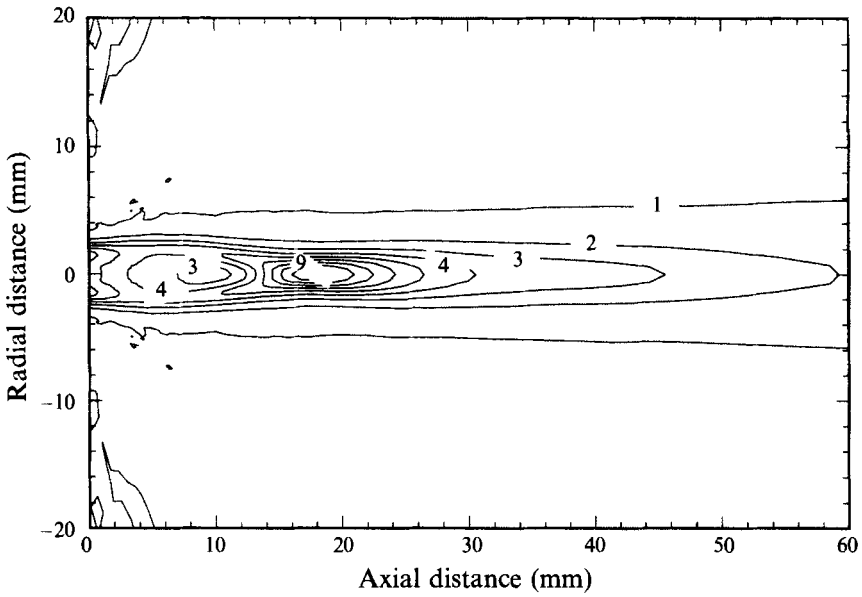


FIGURE 17. Contours of number density in molecules $m^{-3}$ at a background pressure of 43 Pa. (Contour levels multiplied by $10^{-22}$.)

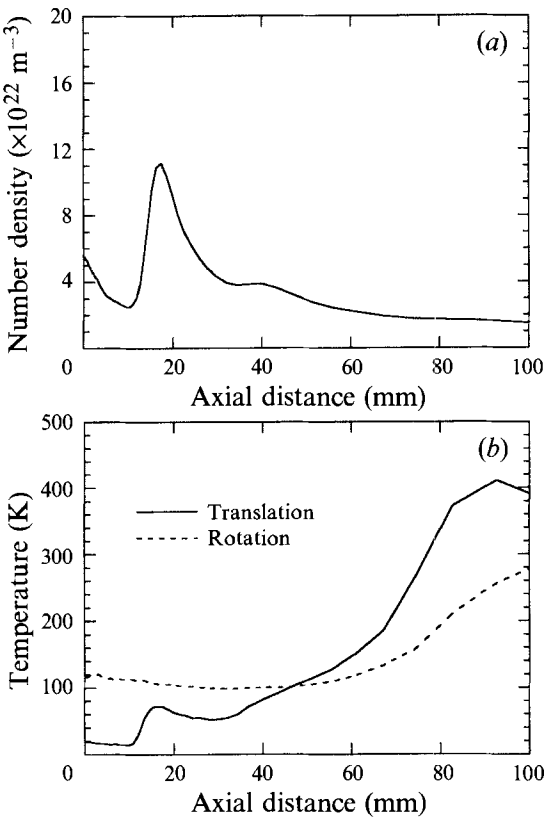


FIGURE 18. (*a*) Number density and (*b*) translational and rotational temperature, along the plume centreline computed with the DSMC method at a background pressure of 43 Pa.

calculations which include the chamber pressure. Careful examination of figure 17 reveals that the density along the jet centreline falls then rises sharply before falling again. This behaviour is considered in greater detail in figures 18(*a*) and 18(*b*) which show the density and temperatures obtained along the centreline. The profiles indicate that complex fluid dynamics processes are at work. A very strong shock wave is formed at a distance of about 10 mm from the nozzle exit plane. Behind this shock, the gas expands rapidly again before a second compression is reached. This secondary shock-like structure is much weaker, and the gas eventually starts to expand again further downstream. Although not clear in figure 18(*a*), a further weaker compression occurs at about 70 mm from the nozzle exit plane. These results are consistent with the diamond shock patterns observed in larger supersonic nozzles. The pressures in the nozzle exit plane are less than the residual pressure of 43 Pa, thus the nozzle is overexpanded. Actual diamond structure is not observed in the calculations. This is presumably due to viscous dissipation at the low densities encountered. The compression and expansion wave behaviour is also found in the translational temperature profile shown in figure 18(*b*). The translational mode reaches a local maximum after the shock formation at 10 mm from the nozzle exit plane. The subsequent expansion is followed by further compression of the temperature up to and beyond the temperature of the background gas. Extension of the flow field beyond 10 cm axially would presumably allow the translational mode to equilibrate with the residual gas. By comparison, the rotational mode undergoes a much slower rate of

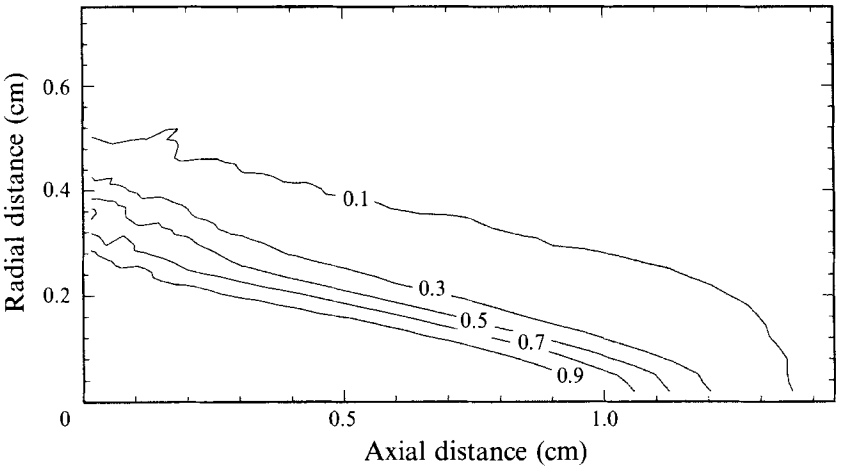


FIGURE 19. Contours of the ratio of pressure obtained at $p_b = 0$ Pa to that obtained at $p_b = 43$ Pa.

relaxation. The rotational temperatures slowly rise towards the equilibrium value. This illustrates the degree of thermal non-equilibrium that accompanies the complex flow-field structure of these interaction regions.

The results shown in figures 18(*a*) and 18(*b*) indicate that the effective test section of flow undisturbed by the residual gas only extends along the axis to a distance of about 10 mm along the plume centreline. Radially, the influence of the chamber pressure is much stronger owing to the reduction in nozzle exit pressure in the radial direction. In figure 19 contours are shown of the ratio of pressures computed with $p_b = 0$ to those obtained at $p_b = 43$ Pa. The contour value just less than unity indicates where the residual gas first affects the plume expansion process. While the flow along the axis is unaffected to a distance of about 10 mm from the nozzle, it is clear that in the radial direction interference effects are felt much sooner. Indeed, it appears that there is some interference close to the nozzle lip in the nozzle exit plane. This is confirmed in figures 20(*a*) and 20(*b*) which compare the number-density and translational-temperature profiles computed just downstream of the nozzle exit plane for the vacuum and $p_b = 43$ Pa cases. Figure 20(*a*) indicates that the number density at the nozzle exit is only slightly affected by the back pressure beyond about 4 mm. The translational temperature, however, is much more sensitive as indicated by figure 20(*b*). The effect of the residual gas is first felt at a radial distance of 3 mm from the centreline.

Consideration is now given to comparison of the numerical results with the measured data. To facilitate taking high-spatial-resolution experimental data, only the density in the $J = 1$ rotational state is measured. These measurements are taken along the plume centreline. In the present study, the corresponding numerical prediction is calculated using the DSMC results obtained for the total number density and the rotational temperature. These are combined in the usual equilibrium relation to determine the number density in the first rotational level. The numerical and experimental results are compared in figure 21. It should be noted that each experimental data point is obtained over a volume that is 4 mm in length axially. The measurements resemble the variation in total number density shown in figure 18(*a*). The agreement between the two data sets is remarkably good. Although the computed shock location is further from the nozzle exit, the peak value is well predicted. While difficult to discern in the experimental data, the secondary compression predicted

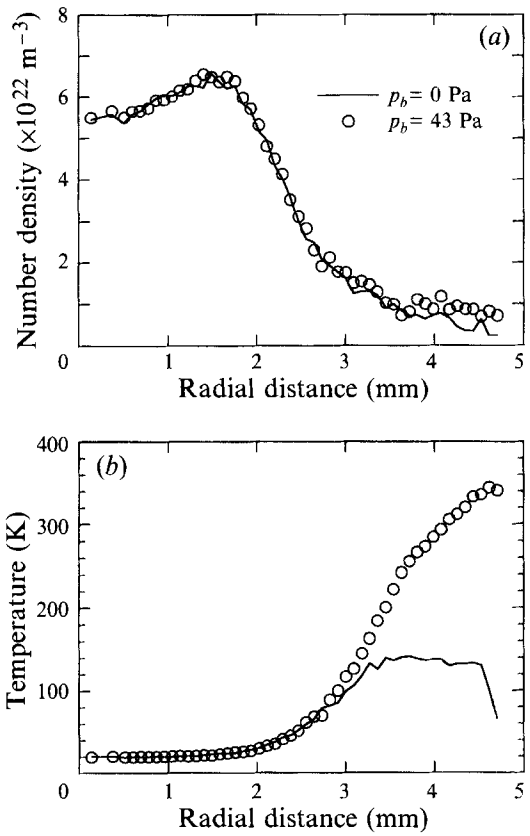


FIGURE 20. Comparison of radial profiles for (*a*) number density and (*b*) temperature, near the nozzle exit plane obtained in vacuum and at finite back pressure.

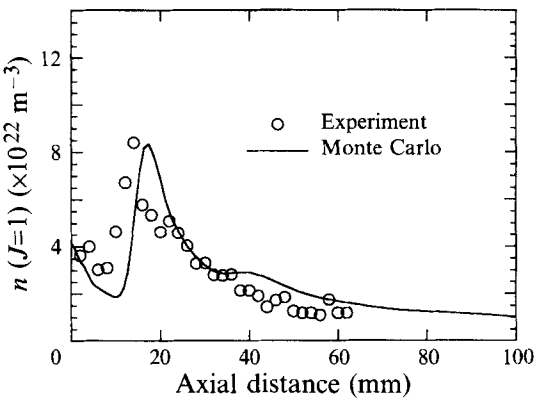


FIGURE 21. Comparison of measured and calculated data for the density of the $J = 1$ state along the plume centreline at a background pressure of 43 Pa.

numerically is not inconsistent with the measurements. Given the complicated fluid mechanics and physics of these flows, and the uncertainty in the spatial distribution of the residual pressure, this degree of agreement is very satisfying. The most obvious explanation for the difference in shock location is that the back pressure is higher at the DSMC boundaries than at the measuring point, which is further downstream. This

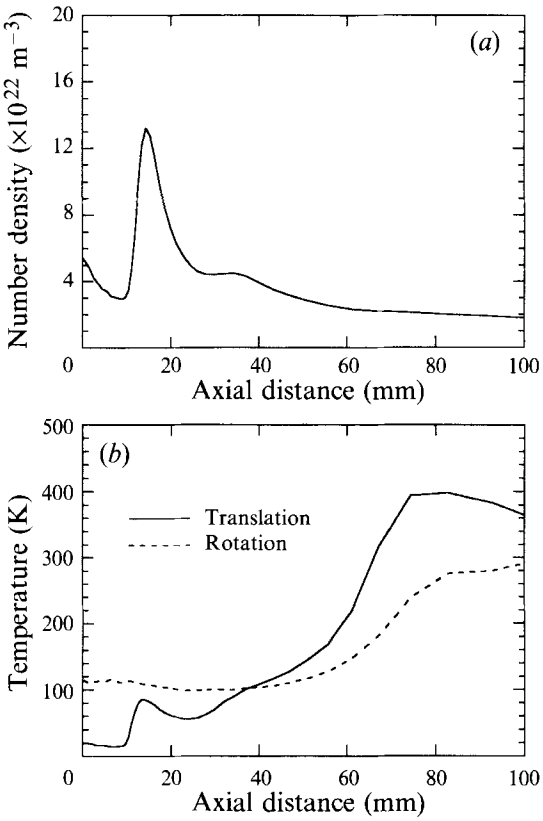


FIGURE 22. (*a*) Number density and (*b*) translational and rotational temperature, along the plume centreline computed with the DSMC method at a background pressure of 56 Pa.

difference would move the shock position back in the simulation slightly downstream of the measured position. It is certainly possible that, locally along the axis, the back pressure may be higher than the value measured experimentally, thus pushing the shock closer to the nozzle exit. It would be difficult to include this type of behaviour in the numerical analysis.

The results obtained at higher residual pressures in the test chamber are now considered. The density and temperature profiles for $p_b = 56$ Pa computed along the plume centreline are shown in figures 22(*a*) and 22(*b*). The results show the same trends as those obtained for the lower value of $p_b$. The shock is moved closer to the nozzle exit plane, and is now stronger. The peak in translational temperature is reached sooner. Comparison with the experimental data shown in figure 23 is once again very good. As before, the precise shock location is predicted slightly further downstream than that measured. Finally, the results obtained at the highest back pressure ($p_b = 67$ Pa) are shown in figures 24(*a*), 24(*b*), and 25. Comparison to the previous figures clearly illustrates the progressive increase in shock strength and movement of the shock closer to the nozzle exit plane as the back pressure is increased. In all these simulations, the DSMC shock-location prediction is slightly further from the nozzle than that observed experimentally. This gives a trend that is consistent with the idea proposed earlier that the pressure set at the DSMC boundaries may be too low since the chamber back pressure is actually measured further downstream of the nozzle. The general agreement between calculation and experiment is maintained. For the experimental data shown

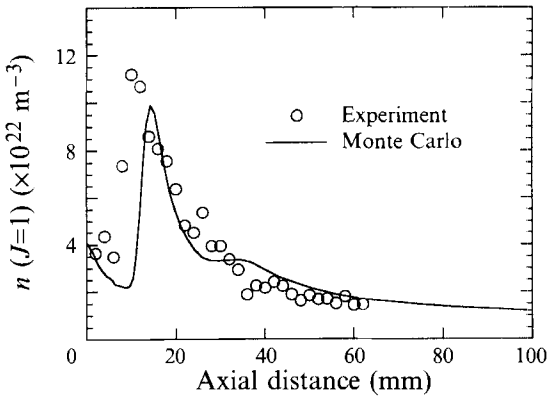


FIGURE 23. Comparison of measured and calculated data for the density of the $J = 1$ state along the plume centreline at a background pressure of 56 Pa.

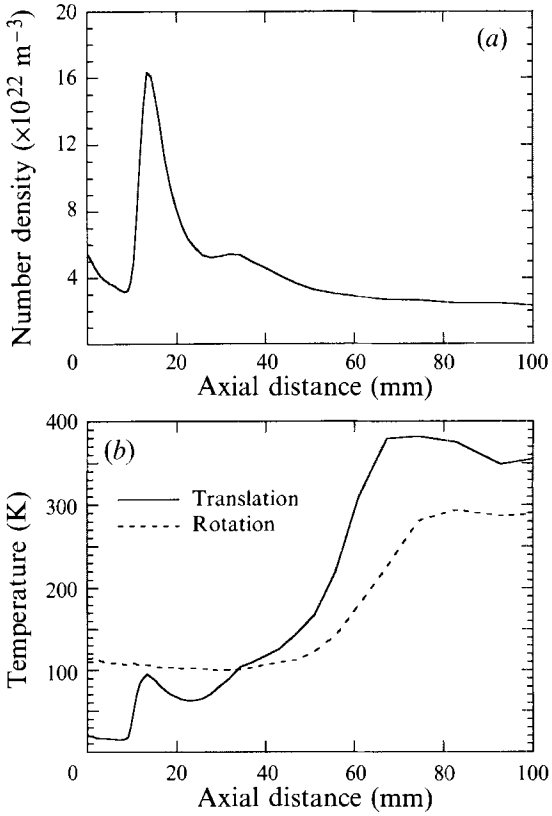


FIGURE 24. (*a*) Number density and (*b*) translational and rotational temperature, along the plume centreline computed with the DSMC method at a background pressure of 67 Pa.

in figure 25 it appears that the measurements at the nozzle exit plane are affected by the back pressure. Clearly, operation of the facility at higher pressures will produce a flow that is not anywhere representative of the plume expanding from the thruster under flight conditions. Simulation of flows at higher values of $p_b$ would require

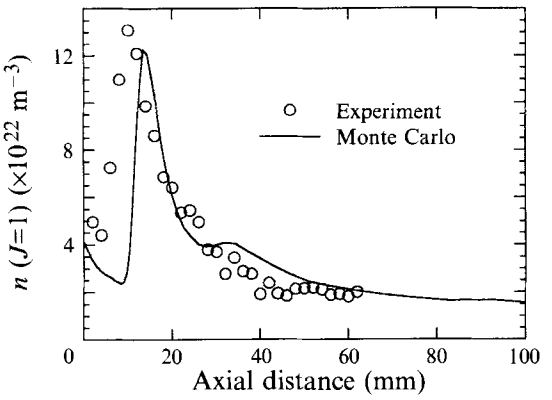


FIGURE 25. Comparison of measured and calculated data for the density of the $J = 1$ state along the plume centreline at a background pressure of 67 Pa.

| Rankine–Hugoniot | $p_b = 43$ Pa | $p_b = 56$ Pa | $p_b = 67$ Pa |
|---|---|---|---|
| 5.74 | 4.47 | 4.79 | 5.19 |

TABLE 3. Density ratio across first shock wave in jet expansion

simultaneous computation of the nozzle and plume flows. At $p_b = 67$ Pa, there is a small amount of flow of the residual gas into the nozzle. This is considered a second-order effect for the results presented. However, at higher pressure, this flow would become more significant and could lead to a region of separated flow inside the nozzle.

It is observed in the density profiles along the jet centreline that when the chamber pressure is increased the shock strength also increases. It is informative to compare the rise in density across the first shock wave predicted by the DSMC method for each value of $p_b$ with the continuum Rankine–Hugoniot theory. At the point where the density first starts to rise in figures 18(*a*), 22(*a*), and 24(*a*), the local Mach number is about 10. The Rankine–Hugoniot theory predicts a density ratio $(\rho_2/\rho_1)$ across a normal shock for a diatomic species of 5.74 at this condition. Each of the density rises obtained from the three DSMC simulations is listed in table 3. As the residual pressure is increased, the density ratio increases and approaches the theoretical value. The density rise in the expanding flow is lower than that predicted by theory owing to non-equilibrium and viscous effects. At the onset of the density rise, there is strong thermal non-equilibrium between the translational and rotational modes. Through the shock wave, low-density collisional effects give rise to non-continuum behaviour. While similar in nature, these flow-field structures are not Mach disks: the flow remains supersonic downstream of the maximum density.

A final note concerns the computational resources required to perform the plume simulations reported here. The solution times required by the DSMC method for the calculations with finite back pressures increase with $p_b$. For the most expensive case of $p_b = 67$ Pa, a total of 15 h on a work-station is required. The simulation of expansion into vacuum is the least expensive and requires about 3 h.

## 5. Conclusions

Advanced numerical and experimental methods were applied to investigate the low-density supersonic flow of a hydrogen jet. For the nozzle flow, it was found that the flow is in strong rotational non-equilibrium. A new rotational model was developed for the Monte Carlo method that was employed to compute the flow field. Computation of rotational temperature in the nozzle exit plane was found to be sensitive to the rate of rotational relaxation employed in the simulation. Comparison of the computed results with the experimental data was quite good and permitted the rotational relaxation time for hydrogen to be estimated. Fine details in the flow field, such as a small decrease in density and corresponding small increase in rotational temperature on the axis in the nozzle exit plane, were observed in both simulation and experiment. It was concluded that the Monte Carlo technique offers accurate prediction of the non-equilibrium flows produced in small nozzles used for low-thrust propulsion applications.

Detailed experimental and numerical results were also obtained for the interaction region of the hydrogen thruster plume expanding into a finite back pressure. Despite the low densities involved, the characteristic phenomena involving formation of shock and expansion waves were observed. Direct comparison of the experimental data and numerical results gave very good agreement along the plume centreline. There were two significant findings from this portion of the present study. First, for this particular facility, there was only a small region of the plume centreline that was unaffected by the back pressure. At the lowest pressures achieved, this region extended to 10 mm along the centreline: this was less than 3 nozzle diameters. It is likely that interference effects first occurred in the radial direction at a much shorter distance from the nozzle. The second important conclusion was that the DSMC method is a very useful technique for calculation of low-density expanding flows. The complex fluid mechanics combined with strong viscous and non-equilibrium effects makes modelling of these flows challenging. The direct comparisons made in this study with experimental measurements indicated that the DSMC technique is capable of accurately simulating such complicated phenomena. It therefore appears that the method is appropriate for assessing the important question of plume interference effects for similar experimental vacuum facilities.

Support by NASA Lewis Research Center for I.D.B. (Grant NAG3-1451) with Dr P. F. Penko as technical monitor is gratefully acknowledged. The work of D.R.B. and M.A.C. was supported in part by NASA Lewis Research Center with Dr F. M. Curran as technical monitor (Grant NAG3-1040), and by Norton Co. (Grant ACH-116820).

## REFERENCES

BIRD, G. A. 1976 *Molecular Gas Dynamics.* Clarendon.

BIRD, G. A. 1981 Monte Carlo simulation in an engineering context. In *Rarefied Gas Dynamics*, Part 1, pp. 239–255. AIAA.

BOITNOTT, C. A. & WARDER, R. C. 1971 Shock tube measurements of rotational relaxation in hydrogen. *Phys. Fluids* **14**, 2312–2316.

BOYD, I. D. 1990 Analysis of rotational nonequilibrium in standing shock waves of nitrogen. *AIAA J.* **28**, 1997–1999.

BOYD, I. D. 1991 Vectorization of a Monte Carlo method for nonequilibrium gas dynamics. *J. Comput. Phys.* **96**, 411–427.

BOYD, I. D., JAFRY, Y. R. & VANDEN BEUKEL, J. 1994 Particle simulations of helium microthruster flows. *J. Spacecraft* **31**, 271–277.

BOYD, I. D., PENKO, P. F., MEISSNER, D. L. & DEWITT, K. J. 1992 Experimental and numerical investigations of low-density nozzle and plume flows of nitrogen. *AIAA J.* **30**, 2453–2461.

FORD, A. L. & BROWN, J. C. 1973 Rayleigh and Raman cross sections for the hydrogen molecule. *Atomic Data* **5**, 305–313.

GALLAGHER, R. J. & FENN, J. B. 1974 Rotational relaxation of molecular hydrogen. *J. Chem. Phys.* **60**, 3087–3091.

JENNINGS, D. E., RAHN, L. A. & OWYOUNG, A. 1985 Laboratory measurement of the S(9) pure rotation frequency. *Astro. J.* **291**, L15–L18.

LAMBERT, J. D. 1977 *Vibrational and Rotational Relaxation in Gases*. Clarendon.

LENSCH, G. & GRONIG, H. 1977 Experimental determination of rotational relaxation in molecular hydrogen and deuterium. In *Proc. 11th Intl Symp. Shock Tubes and Shock Waves*, pp. 132–139. University of Washington Press.

LUMPKIN, F. E., HAAS, B. L. & BOYD, I. D. 1991 Resolution of differences between collision number definitions in particle and continuum simulations. *Phys. Fluids* A **3**, 2282–2284.

MCQUARRIE, D. A. 1973 *Statistical Thermodynamics*, p. 107. University Science Books.

PARKER, J. G. 1964 Comparison of experimental and theoretical vibrational relaxation times for diatomic gases. *J. Chem. Phys.* **41**, 1600–1609.

PENKO, P. F., BOYD, I. D., MEISSNER, D. L. & DEWITT, K. J. 1993 Measurement and analysis of a small nozzle plume in vacuum. *J. Propulsion* **9**, 646–648.

VALENTINI, J. J. 1987 *Laser Spectroscopy and Its Applications*, p. 516. Marcel Dekker.

VIERS, D. K. & ROSENBLATT, G. M. 1987 Raman line positions in molecular hydrogen: $H_2$, HD, HT, $D_2$, DT, and $T_2$. *J. Mol. Spec.* **121**, 401–419.

WEBER, A. 1973 *The Raman Effect*, vol. 2, p. 732. Marcel Dekker.

WOLNIEWICZ, L. 1983 The $X^1\Sigma_g^+$ state vibration-rotational energies of the $H_2$, HD, and $D_2$ molecules. *J. Chem. Phys.* **78**, 6173–6181.